

FAR-UV SPECTROSCOPIC ANALYSES OF FOUR CENTRAL STARS OF PLANETARY NEBULAE¹

J.E. Herald, L. Bianchi

Department of Physics and Astronomy, The Johns Hopkins University

ABSTRACT

We analyze the Far-UV/UV spectra of four central stars of planetary nebulae with strong wind features — NGC 2371, Abell 78, IC 4776 and NGC 1535, and derive their photospheric and wind parameters by modeling high-resolution FUSE (Far-Ultraviolet Spectroscopic Explorer) data in the Far-UV and HST-STIS and IUE data in the UV with spherical non-LTE line-blanketed model atmospheres. Abell 78 is a hydrogen-deficient transitional [WR]-PG 1159 object, and we find NGC 2371 to be in the same stage, both migrating from the constant-luminosity phase to the white dwarf cooling sequence with $T_{\text{eff}} \simeq 120$ kK, $\dot{M} \simeq 5 \times 10^{-8} M_{\odot} \text{ yr}^{-1}$. NGC 1535 is a “hydrogen-rich” O(H) CSPN, and the exact nature of IC 4776 is ambiguous, although it appears to be helium burning. Both objects lie on the constant-luminosity branch of post-AGB evolution and have $T_{\text{eff}} \simeq 65$ kK, $\dot{M} \simeq 1 \times 10^{-8}$. Thus, both the H-rich and H-deficient channels of PN evolution are represented in our sample. We also investigate the effects of including higher ionization stages of iron (up to Fe X) in the model atmosphere calculations of these hot objects (usually neglected in previous analyses), and find iron to be a useful diagnostic of the stellar parameters in some cases. The Far-UV spectra of all four objects show evidence of hot ($T \sim 300$ K) molecular hydrogen in their circumstellar environments.

Subject headings: stars: atmospheres — stars: Wolf-Rayet — stars: individual (NGC 2371, Abell 78, NGC 1535, IC 4776) — planetary nebulae: general — UV: spectroscopy

¹Based on observations made with the NASA-CNES-CSA Far Ultraviolet Spectroscopic Explorer and data from the MAST archive. FUSE is operated for NASA by the Johns Hopkins University under NASA contract NAS5-32985.

1. INTRODUCTION

After leaving the asymptotic giant branch (AGB), low and intermediate-mass stars become central stars of planetary nebulae (CSPN). The spectral types of the central stars are numerous and diverse (*e.g.*, O, Of, sdO, [WR], [WR]-PG 1159, as well as white dwarf-types), but all of these can be generally divided into two groups based on surface abundances: hydrogen-rich (which show obvious hydrogen lines in their spectra) and hydrogen-deficient (which don't). H-deficient stars are in a post-helium flash, helium-burning phase, while the H-rich stars may be either hydrogen or helium burning. About 10-20 % of CSPN are H-deficient (De Marco & Soker 2002; Koesterke & Werner 1998 and references therein). The two groups are thought to represent different “channels” of CSPN evolution, terminating with either H-rich DA type or He-rich DO type white dwarfs (*e.g.*, Napiwotzki 1999). During the CSPN phase the star sheds mass in the form of a stellar wind as it evolves toward the white dwarf cooling sequence. It is generally believed that the winds of these objects are driven by radiation pressure, as with population-I O-stars and WR stars. If the driving of the wind is mainly dictated by the stellar luminosity, the wind parameters can, in principle, be used to determine the distances to CSPN (Kudritzki et al. 1999; Kudritzki & Puls 2000; Tinkler & Lamers 2002).

The spectra of the majority of the H-deficient class have strong wind signatures, show no photospheric lines and are very similar to those of WC stars — the carbon-rich Wolf-Rayets which are evolved massive stars. The low-mass central stars are termed “[WC]” stars to denote their association with planetary nebulae. “PG 1159”- type stars are extremely hot, H-deficient white dwarf-type objects, thought to represent an entry point onto the white dwarf cooling sequence. They show mainly absorption lines in the optical spectra but possess a few wind lines in the UV. Because PG 1159 objects have similar abundances to [WC] stars and about half of the PG 1159 stars are CSPN (Werner 2001), they are thought to be descendants of the [WC]s. Linking these two classes is a rare group of objects named “[WC]-PG 1159” stars, whose spectra show both emission lines and some absorption lines. Only three definite cases of such stars are known so far: Abell 78, Abell 30 and Longmore 4 (Koesterke 2001). Parthasarathy et al. (1998) have posited that all “weak emission line stars” ([WELS]) are actually [WC]-PG 1159, based on optical spectra, but Werner (2001) cautioned against this statement until better spectra of the sample is available. The H-rich CSPN sample of Mèndez et al. (1988) are similar in that their spectra also feature absorption lines as well as UV wind emission features.

[WC], [WC]-PG 1159, and PG 1159 stars all reside in the same area of the H-R diagram (HRD). In terms of evolution, this region corresponds to the bend where the star leaves the constant-luminosity post-AGB phase and is transitioning to the white dwarf cool-

ing sequence. [WC] and PG 1159 stars lie close to each other in the H-R diagram, yet have very different spectra (in the optical, a [WC] spectrum is littered with strong emission lines, while that of a PG 1159 presents an absorption line spectrum). This suggests a dramatic drop in mass-loss rates over a short time of evolution (Koesterke & Werner 1998). The commonly accepted evolutionary sequence for H-deficient CSPN is: [WC] → [WC]-PG 1159 → PG 1159 → DO WD (Hamann 1996). This sequence spans the time where the stellar winds are in the process of “turning-off”. Therefore, understanding the objects in this part of the H-R diagram is not only a prerequisite for understanding the evolution of central stars, but will also give insight into the driving of stellar winds in general.

In the classification of [WR]-type objects, wind parameters are more fundamental discriminators than stellar temperature (Crowther 1999; Acker & Neiner 2003). As the central star’s winds die down, the wind features in the FUV/UV are the last to fade (Koesterke et al. 1998). Therefore, to estimate accurate parameters of the extended atmospheres this phase is best studied in the FUV/UV. In this paper, we present a FUV/UV-based spectral analysis of four CSPN which show strong wind signatures - NGC 2371, Abell 78, IC 4776, and NGC 1535. We model the FUV/UV spectra of these stars using stellar atmospheres codes to determine the wind parameters such as T_{eff} , \dot{M} , and v_∞ and discuss their evolutionary implications. Abell 78 has been classified as a [WO]-PG 1159 transition object (Mèndez 1991; Crowther et al. 1998), and we argue that NGC 2371 also belongs to this class. NGC 1535 is an O(H) star belonging to the H-rich sample of Mèndez et al. (1988). The FUV spectra of IC 4776 is similar to that of NGC 1535, but we find evidence that this object may be a He-burner. Comparing with evolutionary calculations, our derived parameters place the latter two objects along the constant-luminosity path of the HRD, while the former two lie on the bend marking the transition from that phase to the white dwarf cooling sequence.

This paper is arranged as follows. The observations and data reduction are described in § 2. A comparison of the spectra of the objects is presented in § 3. Our models and parameter determinations are described in § 4. The implications of our results are discussed in § 5 and our conclusions in § 6.

2. OBSERVATIONS AND REDUCTION

The coordinates, radial velocities (v_r) and nebular diameters (θ) of our four sample objects are listed in Table 1 (Tylenda et al. 2003 has measured two angular dimensions for three of the sample PN, corresponding to the semi-major and minor diameters, which we list as “ $\theta_B \times \theta_A$ ”). The data sets utilized in this paper are summarized in Table 2. NGC 2371 and IC 4776 were observed as part of FUSE cycle 1 program P133 (Bianchi). All other

FUV/UV data were retrieved from the MAST archive, including FUSE and STIS archive data of NGC 1535, a Berkeley Extreme and Far-UV Spectrometer (BEFS) archive spectrum of Abell 78, and IUE data of most objects. The reduction of the FUSE data is described in § 2.1.

2.1. FUV Data

FUSE covers the wavelength range of 905–1187 Å at a spectral resolution of $\lesssim 30,000$. It is described by Moos et al. (2000) and its on-orbit performance is discussed by Sahnow et al. (2000). FUSE collects light concurrently in four different channels (LiF1, LiF2, SiC1, and SiC2). Each channel is recorded by two detectors, each divided into two segments (A & B) covering different subsets of the above range with some overlap.

The FUSE spectra were taken using the LWRS ($30'' \times 30''$) aperture. These data, taken in “time-tag” mode, have been calibrated using the most recent FUSE data reduction pipeline, efficiency curves and wavelength solutions (CALFUSE v2.2). We combined the data from different segments, weighting by detector sensitivity, and rebinned them to a uniform dispersion of 0.05 Å (which is probably close to the actual resolution since the data were taken in the early part of the mission). Bad areas of the detectors, and those regimes affected by an instrumental artifact known as “the worm” (FUSE Data Handbook v1.1), were excluded. The flux calibration accuracy of FUSE is $\lesssim 10\%$ (Sahnow et al. 2000).

The BEFS spectra covers a wavelength range of 912–1218 Å with a resolution of ~ 0.33 Å. The calibration and performance are described by Hurwitz (1998).

2.2. UV Data

For most stars, we make use of IUE data, using high-resolution spectrum if available (a high-resolution spectra for NGC 2371 exists, but is of poor quality, so we present the low-resolution data instead). For some stars, there was some disagreement ($\lesssim 30\%$) between the FUV (both FUSE and BEFS) and IUE continuum levels in the regions of overlap (flux calibrations for these instruments are typically accurate to $\sim 10\%$). Because there are no nearby objects that could contribute extra flux in the FUSE aperture, we suspect that the background has been over-subtracted in the IUE spectra since nebular continuum emission is expected (in the case of NGC 1535, the STIS spectra agree perfectly well with the FUSE fluxes, but the IUE fluxes are a factor of ~ 1.2 lower). Therefore we have scaled the UV flux levels to those of the FUV (scaling factors are listed in Table 2).

3. DESCRIPTION OF THE SPECTRA

Fig. 1 displays the combined FUV/UV spectra of our sample (up to 1700 Å, longwards of this, the spectra are mostly featureless). Much of the fine structure between 900—1200 Å is caused by sight-line molecular hydrogen (H_2), and is discussed in § 4.2. As far as stellar features go, the spectra present a sparse landscape. The O VI $\lambda\lambda 1032-38$ feature is most prominent in all cases, and the spectra are arranged from top to bottom in order of decreasing strength of this feature. IC 4776 and NGC 1535 both display S VI $\lambda\lambda 933-44$ in the FUV, however, their UV spectra are different. In the FUV, Abell 78 and NGC 2371 have 3 similar lines but N V $\lambda\lambda 1238-43$ and O V $\lambda 1371$ are strong P-Cygni in Abell 78 while absent in NGC 2371, neither showing S VI but both displaying a P-Cygni feature around 977 Å. This feature is commonly assumed to be C III, however the formation of a C III line in the highly-ionized winds of these objects is hard to explain, and this will be discussed later (§ 5).

C IV $\lambda\lambda 1548-51$ appears in all spectra, although it is relatively weak in NGC 1535. N V $\lambda\lambda 1238-43$ is obviously present in all spectra save that of NGC 2371. O V $\lambda 1371$ is absent in NGC 2371, present as a P-Cygni profile in Abell 78 and NGC 1535, and appears perhaps only in absorption in IC 4776. He II $\lambda 1640$ appears to be present in the low-resolution IUE spectrum of NGC 2371, but inspection of the one available (noisy) high-resolution IUE spectra for this object (SWP53006) shows the He II $\lambda 1640$ to be at least partly nebular in origin. The absence of transitions from ions of lower ionization potential (*e.g.*, N IV, O IV, or Si IV) indicate the high ionization state of the winds, and high effective temperatures of the central stars.

4. MODELING

The modeling of these spectra consists of three parts: modeling the central star spectrum, the nebular continuum emission longwards of 1200 Å, and the sight-line Hydrogen (atomic and molecular) absorption shortwards. The reddening must also be adjusted concurrently to match the FUV/UV slope. In all four objects, the reddening is low, and not a significant source of uncertainty. Iterations between each are required to achieve a consistent solution. However, we discuss each in turn for clarity.

4.1. The Central Stars

The optical spectrum of these objects shows mainly absorption lines, and some have been modeled using plane-parallel codes (*e.g.*, Abell 78 by Werner et al. 2003, NGC 1535

by Mèndez et al. 1988). In the FUV/UV, the most prominent features are wind lines. The temperatures and wind parameters of some of these objects have been previously determined from plane-parallel analyses in conjunction with wind-line analyses of one or two wind features (such as C IV $\lambda\lambda$ 1548-51 or O VI $\lambda\lambda$ 1332-38 — Koesterke & Werner 1998). Here we derive wind parameters solely from the FUV/UV spectra.

Intense radiation fields, a (relatively) low wind density, and an extended atmosphere invalidate the assumptions of thermodynamic equilibrium and a plane-parallel geometry for the winds of our sample CSPN. To model these winds, we use the non-LTE (NLTE) line-blanketed code CMFGEN of Hillier & Miller (1998, 1999). CMFGEN solves the radiative transfer equation in an extended, spherically-symmetric expanding atmosphere. Originally developed to model the Wolf-Rayet winds, it has been adapted for objects with weaker winds such as O-stars and CSPN as described in Hillier et al. (2003). The detailed workings of the code are explained in the references therein. To summarize, the code solves for the NLTE populations in the co-moving frame of reference. The fundamental photospheric/wind parameters include T_{eff} , R_* , \dot{M} , the elemental abundances and the velocity law (including v_∞). The *stellar radius* (R_*) is taken to be the inner boundary of the model atmosphere (corresponding to a Rosseland optical depth of ~ 20). The temperature at different depths is determined by the *stellar temperature* T_* , related to the luminosity and radius by $L = 4\pi R_*^2 \sigma T_*^4$, whereas the *effective temperature* (T_{eff}) is similarly defined but at a radius corresponding to a Rosseland optical depth of $2/3$ ($R_{2/3}$). The luminosity is conserved at all depths, so $L = 4\pi R_{2/3}^2 \sigma T_{eff}^4$.

The terminal velocity (v_∞) can be estimated from the blue edge of the P-Cygni absorption features, preferably from features that extend further out in the wind (we used C IV $\lambda\lambda$ 1548-51 primarily). We assume what is essentially a standard velocity law $v(r) = v_\infty(1 - r_0/r)^\beta$ where r_0 is roughly equal to R_* . Once a velocity law is specified, the density structure of the wind is then parameterized by the mass-loss rate through the equation of continuity: $\dot{M} = 4\pi R_*^2 \rho(r) v(r)$.

It has been found that models with the same *transformed radius* R_t [$\propto R_*(v_\infty/\dot{M})^{2/3}$] (Schmutz et al. 1989) and v_∞ have the same ionization structure, temperature stratification (aside from a scaling by R_*) and spectra (aside from a scaling of the absolute flux by R_*^{-2} — Schmutz et al. 1989; Hamann et al. 1993). Thus, once the velocity law and abundances are set, one parameter may be fixed (say R_*) and parameter space can then be explored by varying only the other two parameters (e.g., \dot{M} and T_{eff}). R_t can be thought of as an optical depth parameter, as the optical depth of the wind scales as $\propto R_t^{-2}$, for opacities which are proportional to the square of the density. Scaling the model to the observed flux yields R_*/D — a distance D must be adopted to determine R_* .

For the model ions, CMFGEN utilizes the concept of “superlevels”, whereby levels of similar energies are grouped together and treated as a single level in the rate equations (Hillier & Miller 1998). Ions and the number of levels and superlevels included in the model calculations, as well references to the atomic data, are given in the Appendix (§ A).

4.1.1. *Clumping*

Radiation driven winds have been shown to be inherently unstable (Owocki et al. 1988, 1994), which should lead to the formation of clumps in the expanding atmosphere. The degree of clumpiness is parametrized by f , the *filling factor*. One actually can only derive $\dot{M}_S = (\dot{M}_C / \sqrt{f})$ from the models, where \dot{M}_S and \dot{M}_C are the smooth and clumped mass-loss rates. For the denser winds of population-I Wolf-Rayet stars, the clumping factor can be constrained by the strength of the electron scattered optical line wings, and clumping factors of $f \sim 0.1$ are typical (a reduction of \dot{M} to roughly a third of its smooth value). For O-stars, the lower mass loss rates make the electron scattering effects small and difficult to constrain (Hillier et al. 2003). The winds of our sample stars are even weaker, and we do not attempt to determine the clumping for our sample. Unless otherwise noted, we have adopted $f = 1$ and use \dot{M} to refer to the smooth mass loss rate throughout this paper. This can be seen as an upper limit. One expects the clumping in the more tenuous CSPN wind to be less severe than in a WR wind, so a conservative estimate of the lower limit of \dot{M} would be a third of this value.

4.1.2. *Gravity*

Because of the FUV/UV range contains mostly wind lines, there are no suitable absorption lines to be used as gravity diagnostics. In CMFGEN, gravity enters through the scale height h ($\propto g^{-1}$), which connects the spherically extended hydrostatic outer layers to the wind. The relation between h and g , defined in Hillier et al. (2003), involves the mean ionic mass and mean number of electrons per ion, the local electron temperature and the ratio of radiation pressure to the gravity. Mèndez et al. (1988) determined $\log g = 4.3 \pm 0.2$ for NGC 1535 and Werner et al. (2003) found $\log g = 5.5$ for Abell 78 through analysis of photospheric optical lines. We initially adopted $\log g = 4.3$ for NGC 1535 and IC 4776, and $\log g = 5.5$ for Abell 78 and NGC 2371. For such gravities, the derived wind parameters are not that sensitive to h . Spectral wind features can be fit with the models of the same T_{eff} but with gravities differing by over a magnitude. We discuss the issue of gravity more in § 5.

4.1.3. Abundances

Throughout this work, the nomenclature X_i represents the mass fraction of element i , “ X_{\odot} ” denotes the solar abundance, and our values for “solar” are taken from Gray (1992).

Because of the lack of photospheric lines, we have made assumptions about the abundances of the model atmospheres. We have computed models with two different abundance patterns: solar abundance for all elements (corresponding to H-rich objects) and carbon/oxygen enriched “[WC]-PG 1159”-type abundances, typical of H-deficient CSPN. With respect to the latter, it has been shown that abundances through the [WC] subclasses are about the same (Crowther et al. 2002, 1998), with the spectroscopic differences mainly tied to \dot{M} and T_{eff} (Crowther et al. 2002). Calculations by Herwig (2001) show that these abundances may result when the star experiences a late He-shell flash. The abundances of PG 1159 objects are similar (Górny & Tylenda 2000). Typical measured values are (by mass): $X_{He} = 0.33\text{--}0.80$, $X_C = 0.15\text{--}0.50$, $X_O = 0.06\text{--}0.17$ (Werner 2001). For these reasons, we have assumed a similar abundance pattern for these elements ($X_{He}/X_C/X_O = 0.54/0.36/0.08$), while adopting solar abundances for others (*e.g.*, S, Si, & Fe). The nitrogen abundance in such objects typically ranges from undetectable to $\sim 2\%$ (by mass, see Werner 2001 and references therein). We have adopted a nitrogen abundance of 1% for most of our models. The lone N V $\lambda\lambda 1238\text{--}43$ feature is abundance sensitive, and we do not rely on it strongly as a diagnostic as it is also sensitive to T_{eff} and \dot{M} . We use these abundances in our models of Abell 78 (a [WR]-PG 1159 star) and of NGC 2371, which has a similar FUV spectrum (Fig. 1).

For the H-rich O(H) star NGC 1535, we have adopted solar abundances for all elements. For IC 4776, which displays a similar FUV/UV spectrum, we have computed models with both solar abundances and the above H-deficient “[WC]/PG 1159” abundances. We are able to fit its spectrum adequately with models of both abundances (we will discuss this more in § 4.1.6).

Table 3 shows our final model elemental abundances. For most, our assumed abundances produced adequate fits. Some required adjusting, as described in § 4.1.6 in a case-by-case basis.

4.1.4. Diagnostics

Optimally, one determines T_{eff} by the ionization balance of He or the CNO elements. It is desirable to use diagnostics from many elements to ensure consistency. However, in the FUV/UV spectra of these objects only oxygen shows two ionization stages – O V and O VI.

We find the O VI feature to be mainly insensitive to \dot{M} and moderately sensitive to T_{eff} , however, the possible influence of X-rays on this line make it less than desirable temperature diagnostic (in the O-stars regime, O VI is also sensitive to \dot{M} , but above a sharp threshold, and this line is primarily created by X-rays — Bianchi & Garcia 2002). The other elements (C, N, S) only show one ionization stage. Because of the lack of multiple ionization stages from the same element in the spectra of most of our sample, effective temperatures are mainly derived from the appearance or absence of ions of different ionization potentials. For example, in our cooler objects (IC 4776 and NGC 1535) the absence of low ionization features such as S V(73 eV), P V(65 eV), O IV(77 eV), and N IV(77 eV) places a lower limit on T_{eff} (\sim 55–60 kK from our models) for a wide range of mass-loss rates and abundances. Tinkler & Lamers (2002) find that between 55–70 kK, H-rich CSPN exhibit a large jump in \dot{M} by a factor of 10–100, which they suspect is due to a bi-stability jump. In our models, it is in this temperature range that these previously mentioned ions jump to the next stage, supporting the idea of Vink et al. (2001) that a bi-stability jump at such high temperatures may be due to CNO elements. The presence of S VI in these object’s spectra further constrains the temperature to be below a certain point. Above $T_{eff} \gtrsim 90$ kK, S VII becomes dominant in the outer wind, and a regime is entered in which our “hotter” objects lie (NGC 2371 and Abell 78). Around $T_{eff} \simeq 120$ kK, the winds become too ionized for O V, a discriminator between our two hot objects.

Saturated features (like O VI) are mainly insensitive to the mass-loss rate. We typically use the observed C IV, O V, and S VI lines to constrain \dot{M} . Also, He II $\lambda 1640$ (not observed in most of our sample objects) is used to place upper limits on this parameter. In some cases, we also use the iron spectrum as an additional diagnostic (§ 4.1.5).

4.1.5. Iron

The effects of iron (and other line-blanketing elements) are important to consider in the modeling of hot stars for multiple reasons. It is known that in the modeling of hot stars, the neglect of important line-blanketing elements such as iron can significantly impact the derived parameters. Furthermore, iron features may be used to provide additional diagnostics of stellar parameters (*e.g.*, Herald et al. 2001). Finally, line-blanketing elements such as iron are high sources of opacity in the wind and are thus important in the understanding of how it is driven.

Our sample represents an ideal test-bed for studying the effects of the inclusion of higher ionization stages of iron (*i.e.*, Fe VII–Fe X) in the model atmospheres, which have typically been neglected in previous studies of similar objects. The temperatures of the objects in

our sample span a range where different stages in this sequence dominate. Since Fe IV–Fe X have transitions which occur in the FUV and UV, the wavelength coverage of our spectral data is adequate to study these effects.

The ionization structures of iron for models in the temperature range of our sample (with similar mass-loss rates) are shown in Fig. 2. The figures illustrate what ionization stages are dominant in various temperature regimes. For the cooler objects, Fe VI–Fe VII dominate. As T_{eff} increases, Fe VIII becomes dominant throughout the wind (between $T_{eff} \gtrsim 100$ kK) and at the highest temperatures ($T_{eff} \gtrsim 120$ kK) Fe IX becomes important in the inner winds layers. Useful iron diagnostics include the array of Fe V transitions occurring between 1350–1500 Å, and the forest of Fe VI–Fe VII lines between 1250 and 1500 Å. Fig. 3 demonstrates how the iron spectrum can be used as a diagnostic of wind parameters for NGC 1535.

4.1.6. Stellar Modeling Results

Our model fits are shown in Fig. 4. We now discuss our results for the individual objects, along with some notes. Our derived stellar parameters and a global discussion is given in § 5.

NGC 1535: The strongest wind features (S VI, O VI, N V, O V, C IV) of this O(H) star are all well fit by our model using solar abundances. As discussed in § 4.1.5, the iron spectrum provides an additional constraint for this O(H) star, as at higher temperatures the Fe VII features are too strong (reducing \dot{M} serves to weaken the non-iron wind features to unacceptable levels).

Our derived parameters ($T_{eff} = 66 \pm 5$ kK, $\log \dot{M} = -8.10 \pm 0.3$ $M_{\odot} \text{ yr}^{-1}$) agree within the uncertainties with those of Koesterke et al. (2004), who model this object using a different wind code ($T_{eff} = 70$ kK, $\log \dot{M} = -7.8$ $M_{\odot} \text{ yr}^{-1}$). The temperature is about the same as that found by Mèndez et al. (1988) in their plane-parallel analysis of optical spectra ($T_{eff} = 58 \pm 5$ kK, $\log g = 4.3 \pm 0.2$). It is cooler than that derived by Tinkler & Lamers (2002) who reported the following parameters for NGC 1535: $T_{eff} = 80$ kK, $R_* = 0.38 R_{\odot}$, $\log L = 3.76 L_{\odot}$, $\log g = 5.05$, $v_{\infty} = 1900 \text{ km s}^{-1}$, and $\log \dot{M} = -8.7 \pm 0.7$ $M_{\odot} \text{ yr}^{-1}$ ($R_t = 430_{-280}^{+570}$). Their mass-loss rate, which is about a factor of 4 lower than ours, was derived solely from O V $\lambda 1371$, which we find is quite sensitive to T_{eff} in this temperature range.

IC 4776: The nebular continuum for this object strongly contributes to the observed UV spectrum at longer wavelengths (§ 4.3). We are able to achieve fits of about the same quality

for this object using either our H-rich or H-deficient abundances by adjusting T_{eff} within the range 55–70 kK and $\log \dot{M}$ within -7.85 ± 0.30 $M_{\odot} \text{ yr}^{-1}$, with the H-rich models yielding slightly better fits (it is our H-rich model which we present in the figures). O VI 1032-38 is a bit weak at $T_{eff} \simeq 60$, but fits well at $T_{eff} = 70$ kK. The S VI 933-44 absorption is too strong in our presented model. It is better fit with the lower limit of our mass-loss rate, but the other wind features are then a bit weak. Our models of either H-rich and H-deficient abundances overproduce O V $\lambda 1371$, which is weak at best in the observations. Cooler models bring in (unobserved) O IV features and lower mass-loss rates weaken all other features. Reducing the oxygen abundance to 1/100th solar brings the feature in line with observations, but then the O VI doublet in the FUV range is far too weak. Bouret et al. (2003) had difficulties fitting this feature in O dwarf stars, which have mass-loss rates of order $10^{-9} - 10^{-6} M_{\odot} \text{ yr}^{-1}$ and are cooler ($T_{eff} \simeq 40 - 50$ kK). They found a very clumped wind ($f = 0.01$) alleviated the problem somewhat.

Our mass-loss rates also agree with the predictions we obtained using the Vink et al. (2001) prescription (§ 5), which uses normal (*i.e.*, non-He or C enriched) abundances. The low mass-loss rate of these objects and the dearth of diagnostics make the abundances difficult to constrain, and from our analysis, we cannot tell if IC 4776 is H-rich or H-deficient. Comparison with the evolutionary tracks (also see § 5) indicate this object is most probably a He-burner.

IC 4776 has been classified as a [WC6] star (Feibelman 1999) and as a “weak emission lined object” (a WELS — Tylenda et al. 1993). The [WC6] classification for IC 4776 was based on the equivalent width of C III $\lambda 2297$. This classification is questionable for the following reasons. The spectra of a [WC5] or [WC6] object should contain relatively strong C III features throughout its spectrum (*e.g.*, Crowther et al. 1998; Hillier & Miller 1999), whereas the FUV/UV spectrum of IC4776 is relatively featureless. The FUSE spectrum of this object shows high ionization features such as O VI and S VI, and indicating a state of higher ionization than one would expect in a [WC6] object.

Abell 78: The prominent wind lines of this object (O VI, N V, O V, C IV) are all well-reproduced by our model, with the exception of the strong P-Cygni feature at the location of C III $\lambda 977$. Koesterke & Werner (1998) also had problems reproducing this feature in Abell 78, and speculated that neglected iron lines might sufficiently cool the outer layers of the (otherwise hot) wind to allow for the formation of C III. However, we have tested models accounting for ionization stages of iron up to Fe X and had no success (the dominant ionization stages in the model winds for these objects are Fe VIII and Fe IX). As iron is likely depleted in this object (see below), this is probably not the solution (although cooling from other species is possible).

Using a solar value for the iron abundance ($[\text{Fe}]=7.67$), we could not simultaneously fit the iron spectrum and our other diagnostic lines. For any appreciable mass-loss rate, relatively strong (unobserved) iron P-Cygni features are seen in models with temperatures spanning ~ 70 – 130 kK. For lower temperatures ($T_{\text{eff}} \lesssim 95$ kK), the set of Fe VII lines shown in Fig. 3 are seen. The hotter models display strong Fe VIII and/or Fe IX features. This supports the findings of Werner et al. (2003), who found Abell 78 to have an iron abundance of at most ~ 0.03 solar. Using this iron abundance, the model spectrum agrees with the observations. Miksa et al. (2002) have also found iron deficiency in a large sample of PG 1159 stars, the supposed descendants of these transitional objects. Iron deficiencies in these objects may result when material in the He-intershell is exposed to *s*-process nucleosynthesis during a thermally pulsating AGB or post-AGB phase (Lugaro et al. 2003; Herwig et al. 2003).

Koesterke (2001) determined $T_* = 115$ kK, $R_t = 45.2$ R_\odot and $v_\infty = 3750$ km s $^{-1}$ for this object, with mass fractions for C/O/N of 40/15/2 %, respectively. Our parameters are essentially the same (36/8/1), except we derive $v_\infty = 3200 \pm 50$ from the fitting the C IV $\lambda\lambda 1248$ –51. Werner et al. (2003) derived $T_{\text{eff}} = 110$ kK and $\log g = 5.5$, also in line with our determinations.

Abell 78 is the prototype “[WC]-PG 1159” star (Hamann 1996; Koesterke & Werner 1998) and was originally placed in a transition phase between the [WR] and PG 1159 [*i.e.*, O(C)] phases by Mèndez (1991). Crowther et al. (1998) suggested a [WO1]-PG 1159 classification based its high O VI $\lambda 3818$ /C IV $\lambda 5808$ ratio. This object also falls into the category termed “O VI-type CSPN”, distinguished by Smith & Aller (1969) from the [WC] class for having O VI $\lambda\lambda 3811$ –34 as one of their most prominent optical features. Our model parameters (derived solely on the FUV and UV spectral region) adequately reproduces the optical wind features of Abell 78.

Abell 78 is also of interest because it belongs to a small group of PN which have H-poor, dusty ejecta. These nebulae consist of a H-poor shell surrounded by a an outer H-rich region, indicating a 2nd ejection event of H-deficient material during the post-AGB phase (Medina & Peña 2000).

NGC 2371: As can be seen in Fig. 1, the FUV flux of this object is almost identical to that of Abell 78, except the wind lines are more conspicuous and broader, indicating a higher terminal velocity and mass-loss rate. The UV spectrum lacks O V, which, in our models, disappears for $T_{\text{eff}} \gtrsim 115$ – 120 kK. There is a weak signature of N V 1238–43. Because of the low resolution of our data, it is unclear if its origin is nebular or stellar. Assuming the latter, this feature weakens enough to fit the observations in our synthetic spectra for models with $T_{\text{eff}} \gtrsim 125$ kK (it should be kept in mind we have assumed a mass fraction of $X_N = 0.01$

for nitrogen). The iron spectrum further constrains the temperature to be $T_{\text{eff}} \gtrsim 130$ kK, because the Fe IX features in the FUV are too strong for lower T_{eff} . However, if one assumes that this object is iron-deficient as is Abell 78 (see § 4.1.6), this restriction is removed. As with Abell 78, our models fail to reproduce the strong wind feature at 977 Å.

The low resolution IUE spectrum shows He II $\lambda 1640$, but the one high resolution IUE spectrum available shows that at least part of the He II emission is nebular. Our upper limit to the mass-loss rate assumes it is all stellar, and our lower limit assumes no stellar He II line. The high-resolution spectrum also reveals the C IV emission to be partly nebular. The absorption trough appears to be saturated (the high-resolution spectrum is under-exposed, and hence extremely noisy, but around the stronger lines there is enough flux to see these details).

Tylenda et al. (1993) classified NGC 2371 as a [WC3]. However, we find the ionization of the wind too high for such a classification. Our model parameters for NGC 2371 are close to those of Abell 78 (PG 1159-[WO1]), with the former star being a bit hotter with a denser wind. Their synthetic optical spectra are qualitatively similar, and so we suggest a [WO]-PG 1159 classification for NGC 2371, but at a higher state of ionization marked by the absence of O V and the presence of O VI. This classification needs to be confirmed with optical spectra, however.

Kaler et al. (1993) noted a peculiarity with the optical O VI emission features of this star: they consisted of two components, a broad, blended feature (with $v_{\infty} \simeq 3400$ km s $^{-1}$) and two resolved narrower features. It is the only known O VI PNN to display both the broad and narrow O VI features. They believed these narrow features were associated with the wind rather than the nebula, because their long-slit CCD spectrum showed no extension of the narrow O VI features beyond the profile of the CS, confining the O VI formation zone to have a radius of ~ 2000 AU. It appears the O VI $\lambda\lambda 1032-38$ for NGC 2371 also has this two component structure, as shown in Fig. 8. Close inspection reveals a narrow emission line superimposed on top of the broad P-Cygni profile, which could correspond to the blue component of the O VI doublet (at ~ 20 km s $^{-1}$ in the rest wavelength of the star). The red feature may also be present, but H₂ absorption prevents a firm conclusion. These narrow O VI components may be evidence of shocked material in the nebula. Herald & Bianchi (2004) found similar (seemingly nebular) O VI features in the LMC CSPN SMP LMC 62.

In their study of O VI PNN, Stanghellini et al. (1995) have found a correlation between the strength of O VI $\lambda\lambda 3811-3834$ and stellar luminosity. According to the models of our two transition stars, this holds true. Throughout our sample, the O VI 1032-38 feature grows stronger with increasing effective temperature and luminosity.

4.2. Molecular and Atomic Hydrogen

Absorption due to atomic and molecular Hydrogen (H_2) along the sight-line complicates the spectra of these objects in the FUSE range where numerous H_2 transitions from the Lyman ($B^1\Sigma_u^+ - X^1\Sigma_g^+$) and Werner ($C^1\Pi_u^{\pm} - X^1\Sigma_g^+$) sequences lie. Toward a CSPN, this sight-line Hydrogen typically consists of interstellar and circumstellar components. Material comprising the circumstellar $H\,I$ and H_2 presumably was ejected from the star earlier in its history (during the AGB phase), and is thus important from an evolutionary perspective. If hot (*e.g.*, $T \gtrsim 300$ K), a small column density [*e.g.*, $\log(N) \sim 16$ cm $^{-2}$] of H_2 can lead to a complex absorption spectrum, obscuring the underlying stellar spectrum (see Herald & Bianchi 2004, Fig. 5). It is therefore necessary to model the $H\,I$ and H_2 characteristics to discern the underlying stellar spectrum. Our parameter determinations for sight-line $H\,I$ and H_2 are listed in Table 4.

H_2 absorption effects were applied to the model spectrum in the following manner. For a given column density (N) and gas temperature (T), the absorption profile of each line is calculated by multiplying the line core optical depth (τ_0) by the Voigt profile $H(a, x)$ (normalized to unity) where x is the frequency in Doppler units and a is the ratio of the line damping constant to the Doppler width (the “ b ” parameter). The observed flux is then $F_{obs} = \exp[-\tau_0 H(a, x)] \times F_{intrinsic}$. To fit the H_2 spectrum of a given object, we first assume the presence of an interstellar component with $T = 80$ K (corresponding to the mean temperature of the ISM — Hughes et al. 1971) and $v_{turb} = 10$ km s $^{-1}$. The column density of this interstellar component is estimated by fitting the strongest transitions. If absorption features due to higher-energy H_2 transitions are observed, a second, hotter (circumstellar) component is added (see example in Fig. 5). The temperature of the circumstellar component can be determined by the absence/presence of absorption features from transitions of different J states, and the column density by fitting these features. Iteration between fitting the interstellar and circumstellar components are performed, as both contribute to the lower-energy features. We note that our terminology of “circumstellar” and “interstellar” components is a simplification, and basically indicate a “cool” component (assumed interstellar) and “hot” component (assumed circumstellar). However, the column density derived for the cooler “interstellar” component may also include circumstellar H_2 .

In the case of NGC 1535, the H_2 has been previously modeled by Bowers et al. (1995) using ~ 3 Å resolution Hopkins Ultraviolet Telescope. They found the data to be well fit employing either a one-component model of $T = 300$ K or a two component model with $T = 144$ and 500 K. Their upper limit for the circumstellar H_2 column density was $\log N(H_2) = 18.4$ cm $^{-2}$. This is consistent with our findings, in which we have fit the H_2 absorption (see § 4.2) using two components, a cool component [$T = 80$ K, $\log N(H_2) =$

18.7 cm^{-2}] and a hot component [$T = 400 \text{ K}$, $\log N(\text{H}_2) = 16.7 \text{ cm}^{-2}$], thanks to the higher resolution of the FUSE spectra.

H I column densities were determined in a similar fashion by fitting the profiles of the Ly α and/or Ly β features (our primary diagnostic feature is indicated in Table 4). For Abell 78 and NGC 1535, the available high-resolution data of the Ly α line enable the sightline H I to be constrained tightly, as illustrated in Fig. 6. For IC 4776 and NGC 2371, the low-resolution IUE spectra are inadequate for this purpose. For IC 4776, we use the blue side of the Ly β profile, but for NGC 2371, the P-Cygni absorption from the O VI doublet extends far enough blueward that Ly β is obscured. We therefore simply assumed an H I column density of 21.0 for this object for fitting purposes.

4.3. Nebular Continuum

Nebular characteristics, taken from the literature, are shown in Table 5. Also presented are nebular radii (r_{neb}) and dynamic (kinematic) ages $\tau_{dyn} = r_{neb}/v_{exp}$, calculated using the angular sizes from Table 1 and the distances from Table 7. Since some nebulae have angular diameter measurements in two dimensions, we used the average, listed as θ_{adopt} .

To determine if the nebula significantly contributes to the UV flux, nebular continuum emission models were computed accounting for two-photon, H and He recombination, and free-free emission processes. The continuum model parameters are the electron density (n_e), the electron temperature (T_e), the Helium to Hydrogen ratio (He/H) and the doubly to singly ionized Helium ratio ($\text{He}^{2+}/\text{He}^+$). The computed emissivity coefficient of the nebular gas was scaled as an initial approximation to the total flux at the Earth by deriving the emitting volume absolute H β flux $F(\text{H}\beta)$, dereddened using $c_{H\beta} = 1.475 E_{B-V}$. If the nebula was not entirely contained within the aperture used for the observations, the continuum was scaled by an appropriate geometrical factor ($4A/\pi\theta^2$ or $4A/\pi\theta_A\theta_B$ where A is the area of the aperture in square arcseconds). Because the value of $F(\text{H}\beta)$ is very uncertain the continuum model was then re-scaled to match the observed flux.

For NGC 2371, Abell 78, and NGC 1535, the estimated nebular continuum fluxes are $\sim 1\%$, $\lesssim 0.1\%$, and $\lesssim 0.01\%$, respectively, of the observed flux between 1400–1500 Å. These fluxes do not significantly affect the modeling of the stellar spectra. However, the contribution of the nebular continuum emission to the UV spectra of IC 4776 is significant, and is responsible for the shape of the observed spectrum at the longer UV wavelengths. This can be seen in Fig. 7, which shows the UV spectrum of this object along with our stellar and nebular continuum models.

4.4. Reddening

In Table 6, we list reddenings determined from the FUV/UV spectral slope, from our measured H I column densities, and from literature. We discuss each in turn.

For even the coolest objects of our sample, wavelengths above 912 Å lie in the Rayleigh-Jeans tail of the spectral energy distribution. This makes the slope of the FUV/UV continuum insensitive to T_{eff} and mainly dependent on the reddening toward the object. We have thus used the slope of the FUV/UV spectra to constrain E_{B-V} toward three of our objects, for which the nebular continuum contribution is negligible. In doing so, we have used the reddening law of Cardelli et al. (1989) assuming $R_v = 3.1$, the standard Galactic value. Although their work was originally valid only for wavelengths longer than 1250 Å, ongoing work has shown that the law may be safely extended through the FUSE range (G. Clayton 2001, private communication). In the case of IC 4776, the nebular continuum contamination in the UV (§ 4.3) hinders this method. However the FUV spectrum is primarily stellar, and the determination of E_{B-V} was based on this range. The sum of the stellar and nebular components, and the derived E_{B-V} , fit well with the overall wavelength range (900-3000 Å).

Our values determined from the UV slope agree well with those determined from literature values of the logarithmic extinction (at H β) using the relation $c_{H\beta} = 1.475 E_{B-V}$. In all cases, the reddening is very small, and does not affect the results of the stellar modeling.

Finally, we list the reddenings implied by our measured column densities of H I (§ 4.2) using the relationship $\langle N(\text{H I})/E_{B-V} \rangle = 4.8 \times 10^{21} \text{ cm}^{-2} \text{ mag}^{-1}$ (Bohlin et al. 1978), which represents typical conditions in the ISM. This results in significantly higher reddenings than the other two methods, indicating that the derived column density includes a significant amount of *circumstellar* H I, which apparently has a smaller dust-to-H I ratio than that of the ISM. This is similar to our findings for other CSPN (Herald & Bianchi 2002, 2004).

5. RESULTS and DISCUSSION

As discussed in § 4.1, values of $\log g$ were taken or estimated from previous works based on optical spectra (photospheric lines). From our spectral fitting process we determined the distance-independent parameters T_{eff} , R_t , and v_∞ . Once a distance is adopted, R_* was derived by scaling the model flux to the observations, and then L and \dot{M} were determined. Distances to our objects found in the literature derived by various methods show large spreads (*e.g.*, for NGC 1535, 0.8–3.1 kpc — Sabbadin et al. 1984). Most are determined from nebular relations, such as that of the nebular radius to ionized mass. Ciardullo & Jacoby (1999) have shown that, in comparison with distance determinations made from

more reliable methods such as spectroscopic parallax, statistical methods typically are off by a factor of 2 or more. With this in mind, our adopted distances from literature are shown in Table 7, along with the resulting parameters.

The results of comparing the effective temperatures and luminosities of our sample to the evolutionary tracks of Vassiliadis & Wood (1994) are shown in Table 8. They include the core mass (M_c , essentially the current mass), the initial mass of the progenitor (M_{init}), the evolutionary age (τ_{evol}) and the gravity derived using M_c and the radii (Table 7). NGC 1535, the H-rich object, was compared with the H-burning tracks, and lies along the constant-luminosity phase. We used the He-burning tracks for NGC 2371 and Abell 78, which both fall on the bend between the constant-luminosity phase and the WD cooling sequence, as appropriate for their transitional nature. At the temperature of IC 4776, the H-burning tracks extend down to luminosities of $\log L \gtrsim 3.5 \text{ L}_\odot$ (corresponding to the $M_{init} = 1.0 \text{ M}_\odot$ track). The upper limit of our luminosity of IC 4776 ($\log L = 3.2^{+0.27}_{-0.15} \text{ L}_\odot$) does not overlap with the H-burning tracks. The parameters of IC 4776 do, however, fall on the He-burning tracks, which we have used in this case. Which tracks were used are listed in the Table.

In most cases, masses calculated using our derived radii and initially adopted gravities ($\log g = 5.5$ for Abell 78 and NGC 2371, $\log g = 4.3$ for NGC 1535 and IC 4776 — § 4.1.2) are unreasonably low (*i.e.*, $\lesssim 0.5 \text{ M}_\odot$). Gravities computed using the track masses are higher than our adopted values in all cases. The gravities of NGC 2371 and Abell 78 ($\log g = 6.3$ and 5.7, respectively) are good agreement with PG 1159 stars of similar temperatures from the 16-object sample of Miksa et al. (2002). Likewise, the gravities of NGC 1535 and IC 4776 ($\log g = 4.9$ and 5.1) are reasonable for CSPN of these temperatures (*e.g.*, Mèndez et al. 1988). Models with these higher gravities resulted in only slight changes to the stellar parameters, and within the errors quotes in Table 7. Therefore we conclude these higher gravities are more appropriate for our sample than those originally adopted from the literature.

For most of our objects, the dynamic ages (Table 5) are 2-4 times lower than the evolutionary ages. This is not unexpected, as the dynamic age is a lower limit to the post-AGB age, because the nebular expansion increases during the early post-AGB phase and then level off as the nucleus fades (see Sabbadin 1984, Bianchi 1992 and references therein). The exception is Abell 78, which has a larger dynamic age than its evolutionary age ($\tau_{dyn} = 15 \text{ kyr}$ vs. $\tau_{evol} = 10$).

Vink et al. (2001) presented wind models that yield mass-loss rates for given stellar parameters, taking into account opacity shifts in the wind due to different ionization structures at different temperatures. They assume “normal” abundances - *i.e.*, not He or CNO enriched. Although their prescriptions were derived from studies of the winds of (massive)

O and B stars, we applied their prescription using the derived parameters (T_{eff} , L , v_∞ , and $\log g$) of our *low-mass* objects (Table 7), using solar metallicity. The results are listed in Table 7. The predicted mass-loss rate of NGC 1535 (which we fit with normal abundances) is the same as our measured value. For NGC 2371 and Abell 78 (the H-deficient objects), the predicted mass-loss rates are many magnitudes lower than our values. This is probably due to the chemically enriched winds of these objects having much higher opacities. For IC 4776, a predicted mass-loss rate is a magnitude lower than our measured value results. This may be an indication that the wind of IC 4776 has some chemical enrichment, another indication it may be an He-burner.

The mass-loss rates of the H-deficient objects are about a magnitude larger than the H-rich object, and have higher terminal velocities. The more powerful winds of the hotter objects are a consequence of the hydrogen deficiency of the atmosphere, which increases the opacity and thus the efficiency in converting radiative momentum flux into wind momentum flux. A measure of the efficiency of the wind at converting radiative momentum flux to wind momentum flux is the “performance number” $\eta = v_\infty \dot{M}c/L$ (Springmann 1994). The performance number basically measures how many times, on average, each photon scatters in the wind. Performance numbers above unity (the “single scattering limit”) are typical of stars with chemically enriched winds such as WR objects. The performance numbers for our sample are also listed in Table 7, and show the H-rich object having the lowest η , while the two H-deficient objects are above the single-scattering limit. IC 4776 has a performance number of unity, again indicating its wind may be chemically enriched.

6. CONCLUSIONS

We have performed a FUV/UV spectral analyses on four CSPN which display combined absorption and wind line spectra, a sign that the winds of these objects are in the process of switching off. Two objects are H-deficient (NGC 2371 and Abell 78), one is H-rich (NGC 1535), and for one our analysis is inconclusive (IC 4776). Thus both channels of the CSPN phase are represented. We derived the stellar wind parameters of the sample PN by modeling their FUV and UV spectra, where strong wind signatures are seen. NGC 1535 and Abell 78 have been previously analyzed in the optical using plane-parallel models (Werner et al. 2003, Mèndez et al. 1988), and the latter also with wind models (Koesterke & Werner 1998). Our parameters are in good agreement with the previous results.

The most striking feature in all the FUV spectra is the O VI doublet. In massive O-type stars, this ion originates from X-rays due to shocks in the radiatively driven winds (Bianchi & Garcia 2002). We are able to fit this feature in our sample CSPN without the inclusion

of X-rays due to their higher effective temperatures.

Two objects have $T_{eff} \simeq 65$ kK, with $\dot{M} \sim 10^{-8} M_{\odot} \text{ yr}^{-1}$. NGC 1535 has been classified as a Hydrogen-rich O(H) star based on its optical spectrum, and we are able to match its FUV/UV spectrum using solar abundances. From the spectrum of IC 4776, we cannot constrain the abundances, but comparison with evolutionary tracks suggest this object is a He-burner. Our models for these objects show a jump in the ionization structure of the CNO elements (and S and P) between 55-70 kK. It is in this temperature range that Tinkler & Lamers (2002) find that H-rich CSPN exhibit a large jump in \dot{M} by a factor of 10-100, which they suspect is due to such a bi-stability jump. This supports the idea of Vink et al. (2001) that a bi-stability jump at such high temperatures may be due to CNO elements.

The two H-deficient objects Abell 78 and NGC 1271 are significantly hotter ($T_{eff} > 110$ kK), with $\dot{M} \sim 10^{-7} M_{\odot} \text{ yr}^{-1}$. Our derived parameters for the [W01]-PG 1159 star Abell 78 generally agree with those of past analyses. We derive similar parameters for NGC 2371, and suggest that it is a [WR]-PG 1159 also, but its wind is more ionized and shows no O V features (a [WO0]-PG 1159?). We find evidence of iron deficiency in both of these objects, supporting the findings of Werner et al. (2003) in Abell 78 and of Miksa et al. (2002) in PG 1159 stars. They lie on the bend in the theoretical evolutionary tracks between the constant luminosity phase and the WD cooling sequence, having post-AGB ages of 10-15 kyr. For [WC] stars, it seems that as the star evolves away from the post-AGB phase through the [WC] sequence, the temperature and terminal velocity of the wind increase as the wind density decreases (Acker & Neiner 2003).

Except for Abell 78, the post-AGB ages predicted by the evolutionary models are typically 2-4 times lower than their kinematic ages. However, kinematic ages are lower limits to the post-AGB age (as the expansion is slower in the initial phase) thus the actual discrepancy may be smaller.

Our FUV/UV analysis has provided wind parameters for H-rich and H-deficient CSPN at the stage in post-AGB evolution where the winds are fading. However, because a precise determination of the mass is not possible, the objects do not necessarily represent the same evolutionary sequence. This work has also provided information on the interstellar and circumstellar environment from our measurements of the column densities and temperatures of H I and H₂ along the sight-lines. Our determinations of the H I column density and E_{B-V} imply that the relationship between these two quantities in the circumstellar (PN) environment of CSPN differs from that of the ISM, having lower dust-to-gas ratios (probably due to the destruction of dust by the radiation field). The high resolution of the FUSE data allow us to detect hot H₂ associated with the nebulae. For all four objects in our sample, a single component of H₂ gas at typical ISM temperatures (*i.e.*, $T \sim 80$ kK) was not adequate

to fit the absorption spectrum. A second, hotter ($T \sim 300$ kK) component was necessary, which we assume to be associated with the circumstellar environment. With the advent of many FUSE observations of CSPN, it is becoming apparent that hot circumstellar H₂ is not uncommon CSPN at quite different evolutionary stages: from old PN with white dwarf nuclei (Herald & Bianchi 2002) to young, compact PN (Herald & Bianchi 2004). The objects in this paper lie either along the constant luminosity section of the post-AGB evolutionary tracks, or on the transition bend to the WD cooling sequence, and thus represent intermediate stages to the previously mentioned cases. Given the intense UV radiation fields emitted by the CSPN, it is likely that the nebular H₂ exists in clumps, shielded by neutral and ionized hydrogen, as appears to be the case in the Helix nebula (Speck et al. 2002).

We thank John Hillier for his help with the CMFGEN code, and Stephan McCandliss for making his H₂ molecular data available. We are indebted to the members of the Opacity Project and Iron Project and to Bob Kurucz for their continuing efforts to compute accurate atomic data, without which, this project would not have been feasible. We are grateful to the referee, Klaus Werner, for his many constructive comments and suggestions. The SIMBAD database was used for literature searches. This work has been funded by NASA grants NAG 5-9219 (NRA-99-01-LTSA-029), NAG5-10364 and NAG5-10364. The BEFS, STIS and IUE data were obtained from the Multimission Archive (MAST) at the Space Telescope Science Institute (STScI). STScI is operated by the Association of Universities for Research in Astronomy, Inc., under NASA contract NAS5-26555.

A. APPENDIX: MODEL ATOMS

Ions and the number of levels and superlevels included in the model calculations are listed in Table 9. The atomic data come from a variety of sources, with the Opacity Project (Seaton 1987; Opacity Project Team 1995, 1997), the Iron Project (Pradhan et al. 1996; Hummer et al. 1993), Kurucz (1995)² and the Atomic Spectra Database at NIST Physical Laboratory being the principal sources. Much of the Kurucz data were obtained directly from CfA (Kurucz 1988, 2002). Individual sources of atomic data include the following: Zhang & Pradhan (1997), Bautista & Pradhan (1997), Becker & Butler (1995), Butler et al. (1993), Fuhr et al. (1988), Luo & Pradhan (1989), Luo et al. (1989), Mendoza (1983, 1995, private communication), Mendoza et al. (1995), Nussbaumer & Storey (1983, 1984), Peach et al. (1988), Storey (1988, private communication), Tully et al. (1990), and Wiese et al.

²See <http://cfa-www.harvard.edu/amdata/ampdata/amdata.shtml>

(1966, 1969). Unpublished data taken from the Opacity Project include: Fe VI data (Butler, K.), Fe VIII data (Sarah and Storey) and Fe IX and Fe X data (C. Mendoza).

REFERENCES

Acker, A. & Neiner, C. 2003, A&A, 403, 659

Bautista, M. A. & Pradhan, A. K. 1997, A&AS, 126, 365

Becker, S. R. & Butler, K. 1995, A&A, 301, 187

Bianchi, L. 1992, A&A, 260, 314

Bianchi, L. & Garcia, M. 2002, ApJ, 581, 610

Bohlin, R. C., Savage, B. D., & Drake, J. F. 1978, ApJ, 224, 132

Bouret, J.-C., Lanz, T., Hillier, D. J., Heap, S. R., Hubeny, I., Lennon, D. J., Smith, L. J., & Evans, C. J. 2003, ApJ, 595, 1182

Bowers, C. W., Blair, W. P., Long, K. S., & Davidsen, A. F. 1995, ApJ, 444, 748

Butler, K., Mendoza, C., & Zeippen, C. J. 1993, Phys. Rev. B, 26, 4409

Cahn, J. H. & Kaler, J. B. 1971, ApJS, 22, 319

Cahn, J. H., Kaler, J. B., & Stanghellini, L. 1992, A&AS, 94, 399

Cardelli, J. A., Clayton, G. C., & Mathis, J. S. 1989, ApJ, 345, 245

Ciardullo, R. & Jacoby, J. H. 1999, ApJ, 515, 191

Crowther, P. A. 1999, in IAU Symp., Vol. 193, Wolf-Rayet Phenomena in Massive Stars and Starburst Galaxies, ed. K. A. van der Hucht, G. Koenigsberger, & P. R. J. Eenens (San Francisco: ASP), 116

Crowther, P. A., De Marco, O., & Barlow, M. J. 1998, MNRAS, 296, 367

Crowther, P. A., Dessart, L., Hillier, D. J., Abbott, J. B., & Fullerton, A. W. 2002, A&A, 392, 653

De Marco, O. & Soker, N. 2002, PASP, 114, 602

Feibelman, W. A. 1997, ApJ, 112, 193

—. 1999, *ApJ*, 519, 726

Fuhr, J. R., Martin, G. A., & Wiese, W. L. 1988, in *J. Phys. Chem. Ref. Data, Vol. Supp.* 4 (New York: Am. Chem. Soc. & AIP), 17

Gesicki, K. & Zijlstra, A. A. 2000, *A&A*, 358, 1058

Górny, S. K. & Tylenda, R. 2000, *A&A*, 362, 1008

Gray, D. F. 1992, *The Observation and Analysis of Stellar Photospheres* (Cambridge: Cambridge Univ. Press)

Hamann, W.-R. 1996, *Ap&SS*, 238, 31

Hamann, W.-R., Koesterke, L., & Wesselowski, U. 1993, *A&A*, 274, 397

Herald, J. E. & Bianchi, L. 2002, *ApJ*, 581, 434

—. 2004, *ApJ, submitted*

Herald, J. E., Hillier, D. J., & Schulte-Ladbeck, R. E. 2001, *ApJ*, 548, 932

Herwig, F. 2001, *Ap&SS*, 275, 15

Herwig, F., Lugaro, M., & Werner, K. 2003, in *IAU Symp., Vol. 209, Planetary Nebulae: Their Evolution and Role in the Universe*, ed. M. Dopita & S. Kwok (San Francisco: ASP), 85

Hillier, D. J., Lanz, T., Heap, S. R., Hubeny, I., Smith, L. J., Evans, C. J., Lennon, D. J., & Bouret, J. C. 2003, *ApJ*, 588, 1039

Hillier, D. J. & Miller, D. L. 1998, *ApJ*, 496, 407

—. 1999, *ApJ*, 519, 354

Hughes, M. P., Thompson, A. R., & Colvin, R. S. 1971, *ApJS*, 23, 323

Hummer, D. G., Berrington, K. A., & Eissner, W. 1993, *A&A*, 279, 298

Hurwitz, M. 1998, *ApJ*, 500, 1

Kaler, J. B., Stanghellini, L., & Shaw, R. A. 1993, *A&A*, 279, 529

Koesterke, L. 2001, *Ap&SS*, 275, 41

Koesterke, L., Dreizler, S., & Rauch, T. 1998, *A&A*, 330, 1041

Koesterke, L. & Werner, K. 1998, ApJ, 500, 55

Koesterke, L., Werner, K., Kruk, J. W., & Lanz, T. 2004, in Asymmetric Planetary nebulae III; ASP Conference Series, Vol. XXX, ed. M. Meixner, J. Kastner, B. Balick, & N. Soker (San Francisco: ASP), *in press*

Kudritzki, R. P. & Puls, J. 2000, ARA&A, 38, 613

Kudritzki, R. P., Puls, J., & Lennon, D. J., e. a. 1999, A&A, 350, 970

Kurucz, R. L. 1988, in Transactions of the International Astronomical Union, ed. D. R. Schultz, P. S. Krstic, & F. Ownby, Vol. XXB (Dordrecht: Kluwer), 168

Kurucz, R. L. 1995, CD ROM 23, Atomic Line Data (Cambridge: Smithsonian Astrophysical Obs.)

Kurucz, R. L. 2002, in AIP Conf. Proc., Vol. 183, Atomic and Molecular Data and Their Applications, ed. D. R. Schultz, P. S. Krstic, & F. Ownby (Melville: AIP), 636

Lugaro, M., Herwig, F., Lattanzio, J. C., Gallino, R., & Straniero, O. 2003, ApJ, 586, 1305

Luo, D. & Pradhan, A. K. 1989, Phys. Rev. B, 22, 3377

Luo, D., Pradhan, A. K., Saraph, H. E., Storey, P. J., & Yan, Y. 1989, Phys. Rev. B, 22, 389

Medina, S. & Peña, M. 2000, Revista Mexicana de Astronomía y Astrofísica, 36, 121

Mèndez, R. H. 1991, in IAU Symp., Vol. 145, Evolution of Stars: The Photospheric Abundance Connection, ed. G. Michaud & A. Tutukov (The Netherlands: IAU), 375

Mèndez, R. H., Kudritzki, R. P., Herrero, A., Husfeld, D., & Groth, H. G. 1988, A&A, 190, 113

Mendoza, C., Eissner, W., Le Dourneuf, M., & Zeippen, C. J. 1995, Phys. Rev. B, 28, 3485

Miksa, S., Deetjen, J. L., Dreizler, S., Kruk, J. W., Rauch, T., & Werner, K. 2002, A&A, 389, 953

Moos, H. W., Cash, W. C., & Cowie, L. L. 2000, ApJ, 538, 1

Napiwotzki, R. 1999, A&A, 350, 101

Nussbaumer, H. & Storey, P. J. 1983, A&A, 126, 75

—. 1984, A&AS, 56, 293

Opacity Project Team. 1995, The Opacity Project, Vol. 1 (Bristol: Institute of Physics Publications)

—. 1997, The Opacity Project, Vol. 2 (Bristol: Institute of Physics Publications)

Owocki, S. P., Castor, J. I., & Rybicki, G. B. 1988, ApJ, 335, 914

Owocki, S. P., Cranmer, S. R., & Blondin, J. M. 1994, ApJ, 424, 887

Parthasarathy, M., Acker, A., & Stenholm, B. 1998, A&A, 329, 9

Peach, G., Saraph, H. E., & Seaton, M. J. 1988, Phys. Rev. B, 21, 3669

Phillips, J. P. 1998, A&A, 340, 527

Pradhan, A. K., Zhang, H. L., Nahar, S. N., Romano, P., & Baustista, M. A. 1996, BAAS, 189, 7211

Sabbadin, F. 1984, A&AS, 58, 273

Sabbadin, F., A., B., & Hamzaoglu, E. 1984, A&AS, 136, 193

Sahnow, D. J., Moos, M. W., & Ake, T. B. 2000, ApJ, 538, 7

Schmutz, W., Hamann, W.-R., & Wesselowski, U. 1989, A&A, 210, 236

Seaton, M. J. 1987, Phys. Rev. B, 20, 6363

Smith, L. F. & Aller, L. H. 1969, ApJ, 157, 1245

Speck, A. K., Meixner, M., Fong, D., McCullough, P. R., Moser, D. E., & Ueta, T. 2002, ApJ, 123, 346

Springmann, U. 1994, A&A, 289, 505

Stanghellini, L., Kaler, J. B., Shaw, R. A., & di Serego Alighieri, S. 1995, A&A, 302, 211

Tinkler, C. M. & Lamers, H. J. G. L. M. 2002, A&A, 384, 987

Tully, J. A., Seaton, M. J., & Berrington, K. A. 1990, Phys. Rev. B, 23, 3811

Tylenda, R., Acker, A., Raytchev, B., Stenholm, B., & Gleizes, F. 1991, A&AS, 89, 77

Tylenda, R., Acker, A., & Stenholm, B. 1993, A&AS, 102, 595

Tylenda, R., Siòdmiak, N., Gòrny, S. K., Corradi, R. L. M., & Schwarz, H. E. 2003, A&A, 405, 627

Vassiliadis, E. & Wood, P. R. 1994, ApJ, 92, 125

Vink, J. S., de Koter, A., & Lamers, H. J. G. L. M. 2001, A&A, 369, 574

Weinberger, R. 1989, A&AS, 78, 301

Werner, K. 2001, Ap&SS, 275, 27

Werner, K., Dreizler, S., Koesterke, L., & Kruk, J. W. 2003, in IAU Symp., Vol. 209, Planetary Nebulae: Their Evolution and Role in the Universe, ed. M. Dopita & S. Kwok (San Francisco: ASP), 239

Wiese, L. L., Smith, M. W., & Glennon, B. M. 1966, NSRDS-NBS 4, Vol. 1, Atomic Transition Probabilities (Washington, D.C.: US Government Printing Office)

Wiese, L. L., Smith, M. W., & Miles, B. M. 1969, NSRDS-NBS 22, Vol. 2, Atomic Transition Probabilities (Washington, D.C.: US Government Printing Office)

Zhang, H. L. & Pradhan, A. K. 1997, A&AS, 126, 373

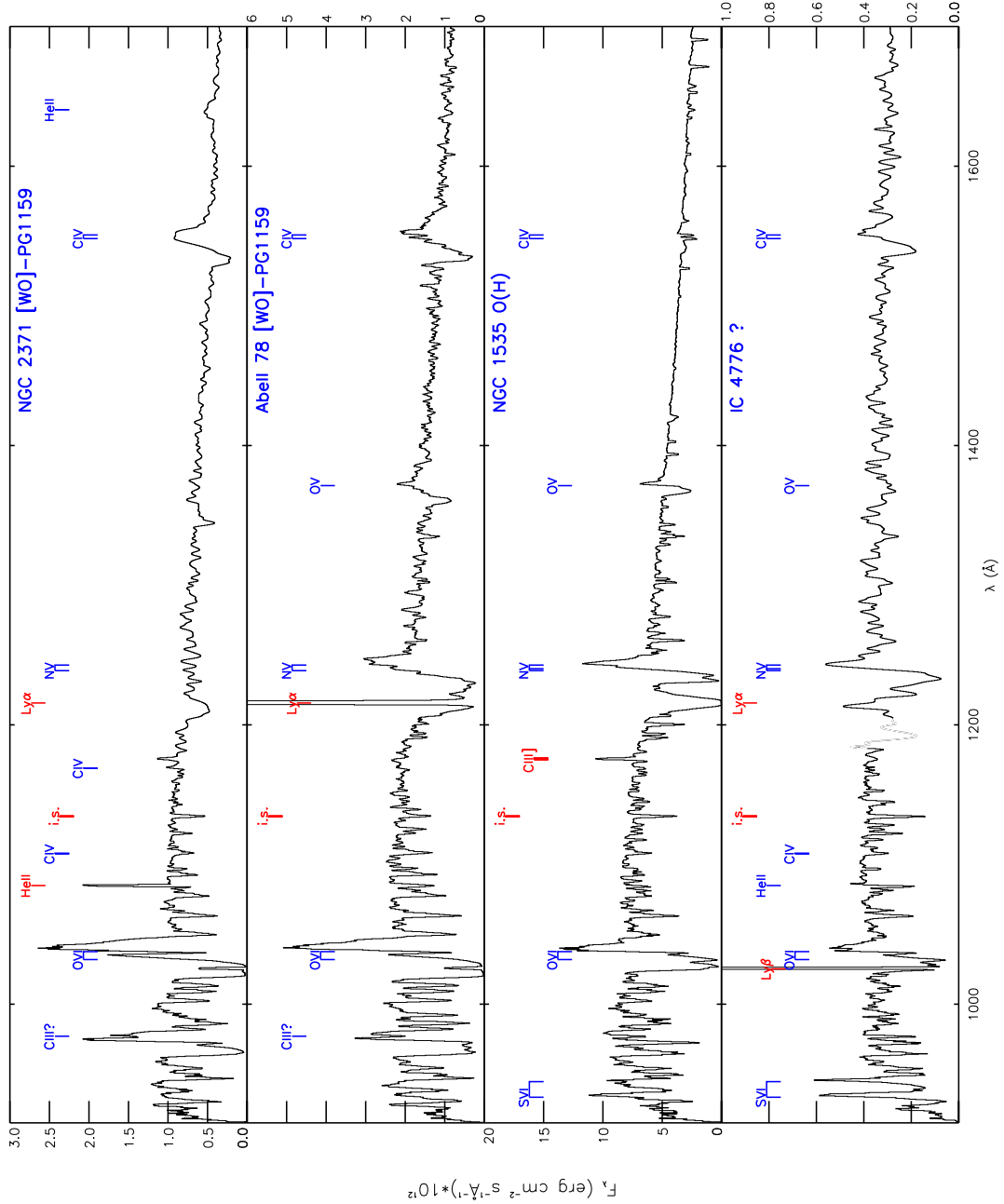


Fig. 1.— FUV/UV spectra of our sample. Data are from different instruments (with different resolutions - see Table 2). The spectrum of IC 4776 appears flatter than the others because of the contribution from the nebular continuum (see § 4.3). Prominent stellar features are marked with dark/blue labels, and interstellar/nebular features by light/red features. Regions of bad data are blanked out.

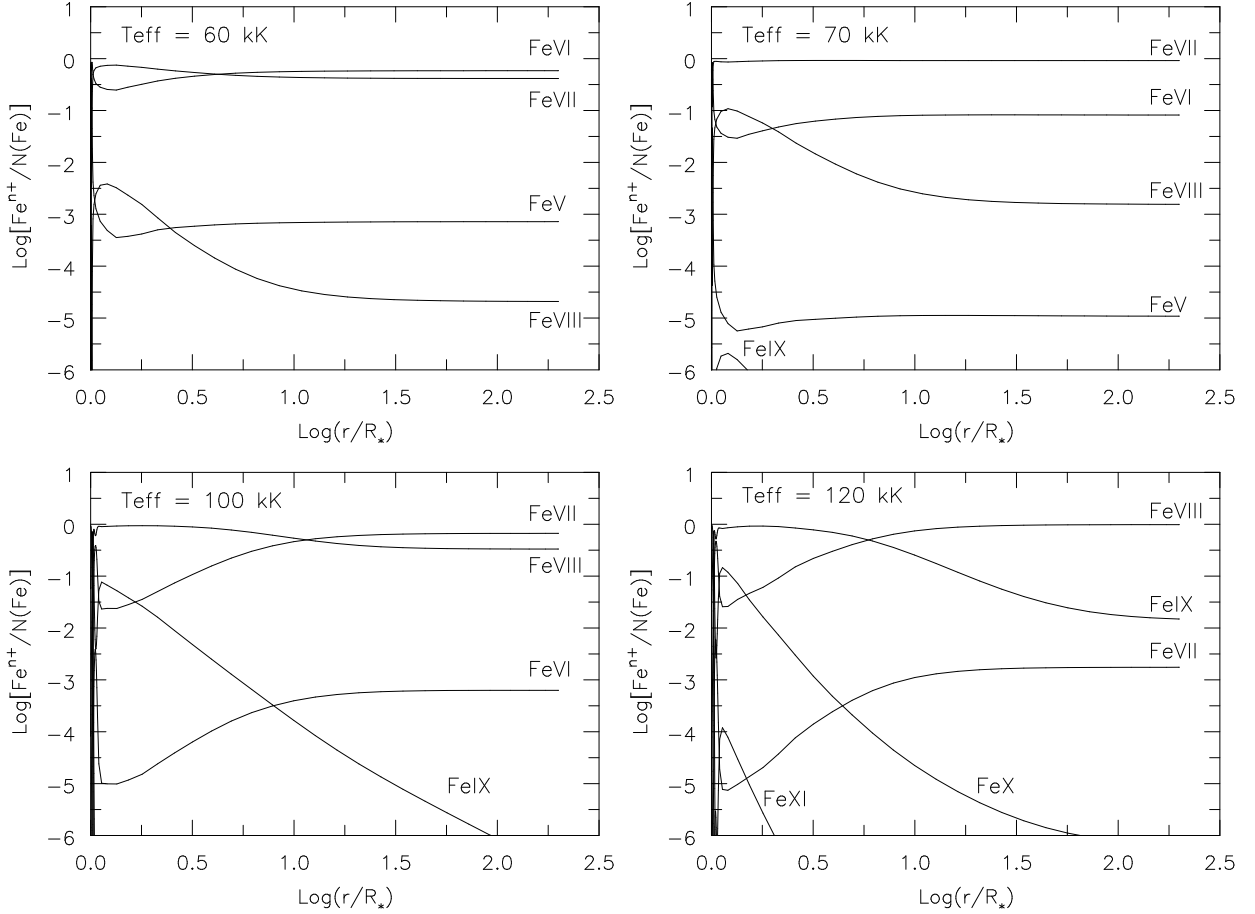


Fig. 2.— The ionization structure of iron for models spanning the temperature ranges of our objects, as a function of distance from the stellar surface. The upper panels are models with temperatures of our cooler objects ($T_{eff} \simeq 60 - 70$ kK), where Fe VI–Fe VII dominate throughout the wind. The lower panels models in the temperature range of our hotter objects ($T_{eff} \simeq 100 - 130$ kK), where the higher ionization stages are dominant. These figures illustrate the sensitivity of the ionization structure of iron to T_{eff} .

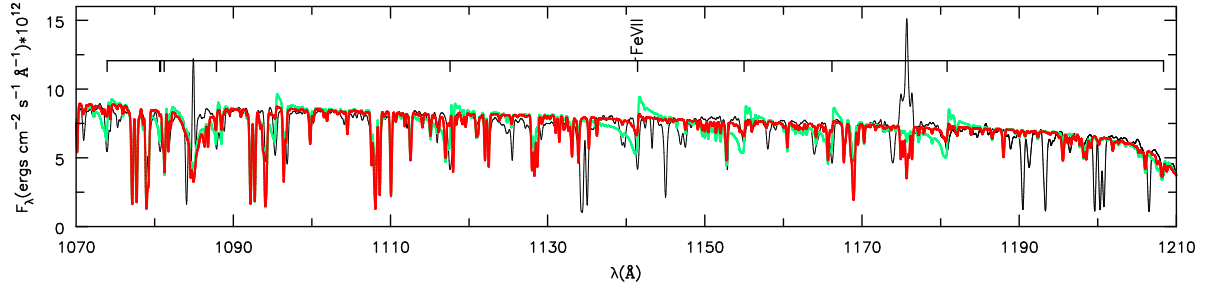


Fig. 3.— NGC 1535: Iron spectrum as a diagnostic. Observations of NGC 1535 are shown (black) along with a model with $T_{eff} \simeq 75 \text{ kK}$, $\dot{M} \simeq 3 \times 10^{-8} \text{ M}_\odot \text{ yr}^{-1}$ (green/light gray). This model displays an Fe VII spectrum stronger than the observations, indicating a lower mass-loss rate and/or a different temperature is required. Our final model, with $T_{eff} \simeq 65 \text{ kK}$, $\dot{M} \simeq 1 \times 10^{-8} \text{ M}_\odot \text{ yr}^{-1}$ (red/heavy gray) provides a better fit.

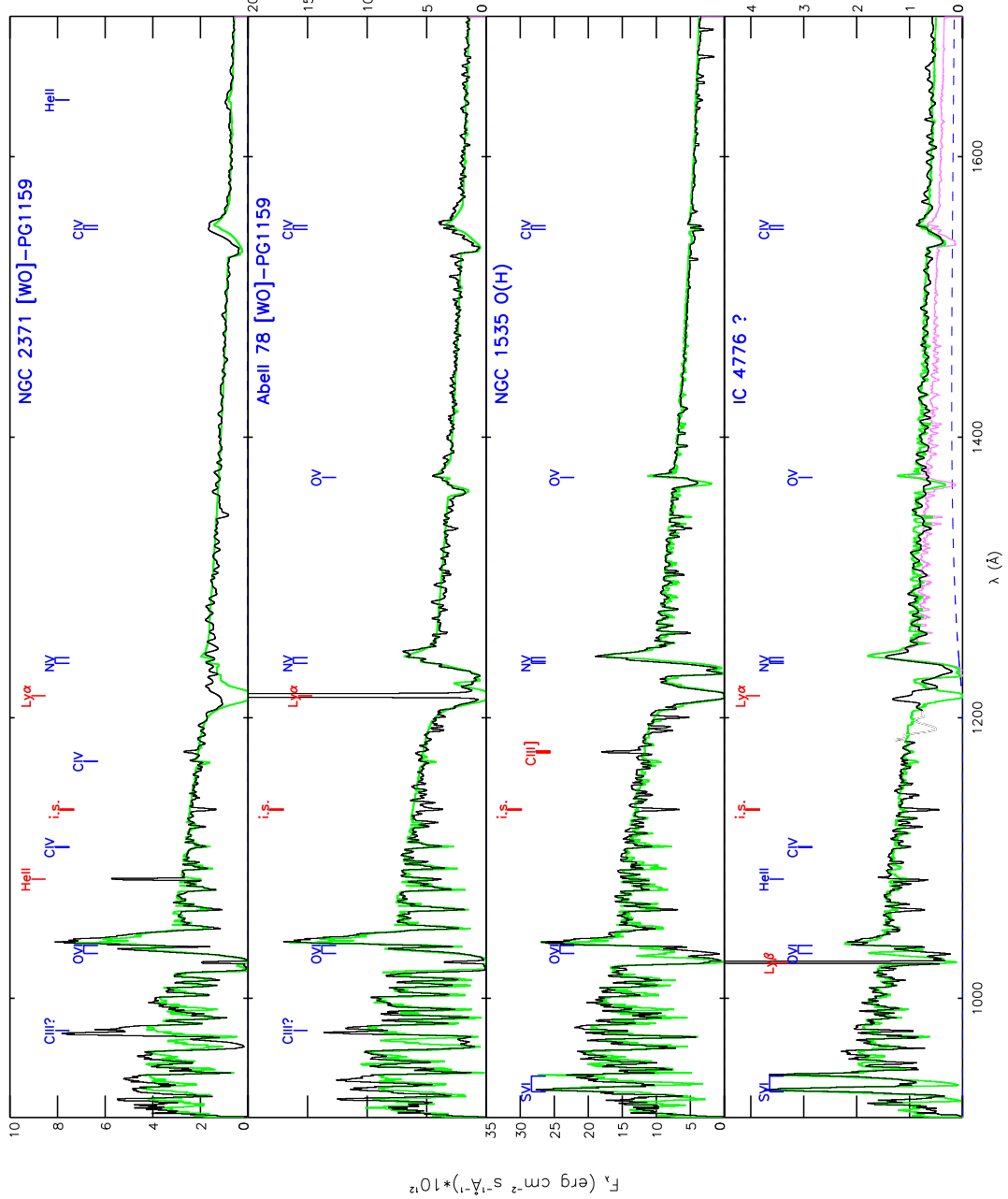


Fig. 4.— Model fits. The observations (black) have been unreddened using our values for E_{B-V} derived from the UV slope, and our models (green/thick gray) are also shown. In the case of IC 4776, the model nebular continuum (blue/dark dashed), and the stellar model (pink/light gray) are summed together (green/thick gray). The prominent wind features are marked with black labels, and strong nebular and interstellar features are marked with gray/red labels. The spectra have been convolved with a 0.75 Å Gaussian for clarity.

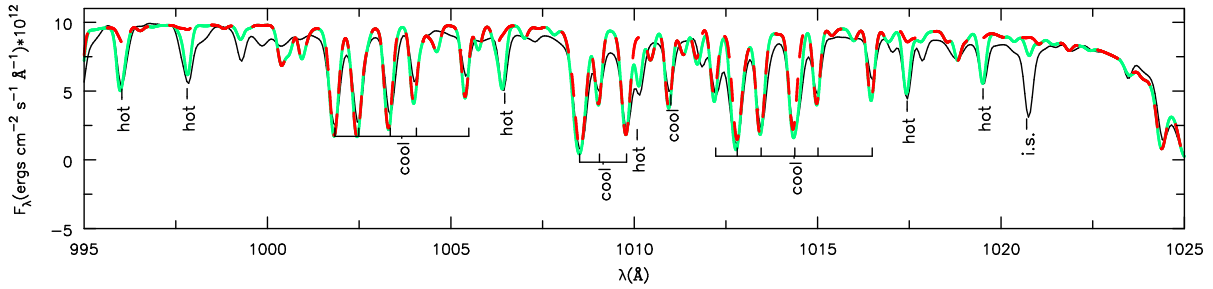


Fig. 5.— Fitting H₂: The FUSE spectrum of NGC 1535 is shown (black) along with a stellar model with successive hydrogen absorption components applied (Table 4). The dashed red/dark gray line shows the stellar model with absorption from the “cool” ($T = 80$ kK) H I and H₂ components applied, and the green/light gray line with absorption effects of the “hot” H₂ component ($T = 400$) H₂ applied to that. Features attributable to the hot and cool hydrogen absorption model is not sufficient to fit all the features, suggesting a hot H₂ gas associated with the nebula.

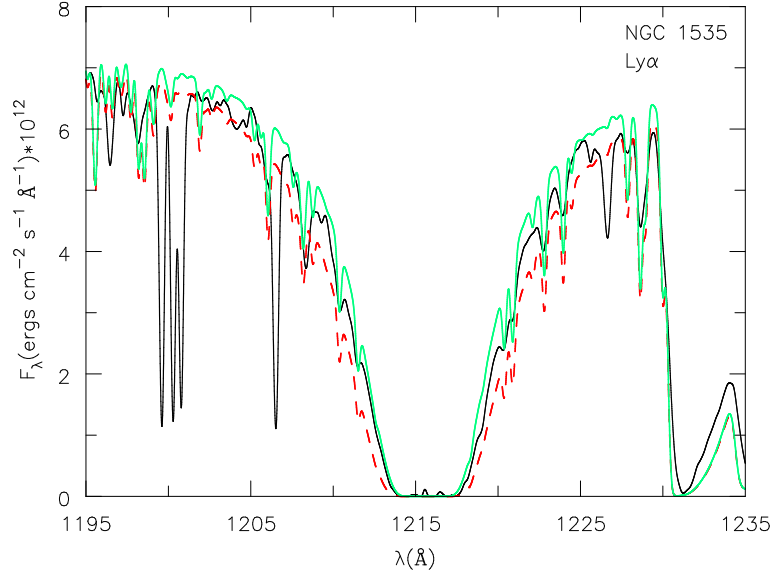


Fig. 6.— Fitting Ly α of NGC 1535: The Ly α profile in the STIS data (black) and our stellar model with the absorption effects of different amounts of H I applied ($T = 80$ kK): column densities of $\log N = 20.8$, (green/light gray) and 21.0 cm^{-2} (dashed red/dark gray). The models bracket the observations, so the sight-line column density can be well constrained to $\log N = 20.8 \pm 0.1$ cm^{-2} .

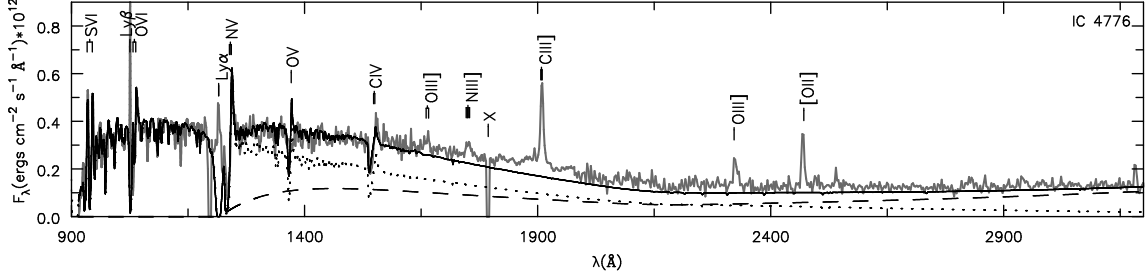


Fig. 7.— IC 4776: The observations are shown (gray) along with our stellar (dotted) and nebular continuum models (dashed). The sum of both models is also shown (solid), demonstrating the flux longwards of Ly α (1215 \AA) of this object is significantly affected by the nebular continuum. We have applied our molecular hydrogen absorption model (§ 4.2) to the stellar model, and our atomic hydrogen absorption model to both the stellar and nebular models. In the FUV, the observations and models have been convolved with a 2 \AA Gaussian for clarity.

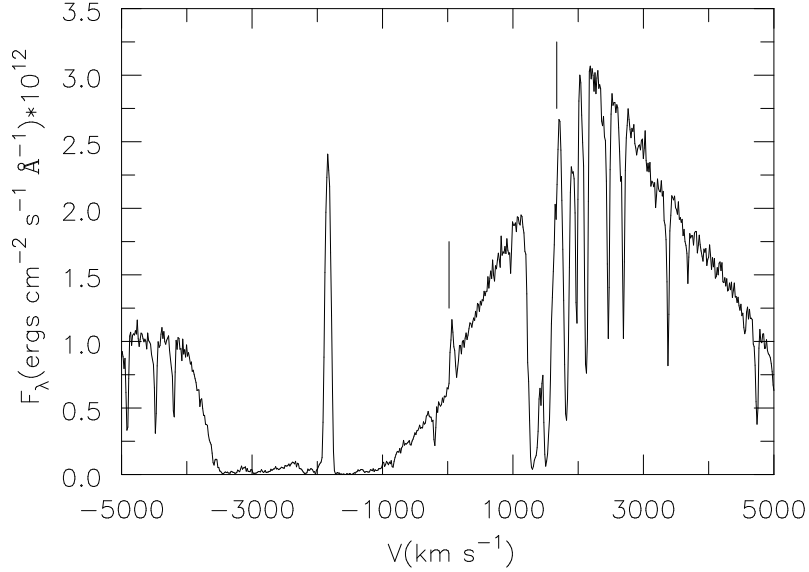


Fig. 8.— O VI $\lambda\lambda 1031.93, 1037.62$ for NGC 2371, in velocity space around 1031.93Å. The spectra has been blueshifted to account for the measured radial velocity of the star of $v_r = +20.6$ km s $^{-1}$ (Table 1). Marked is a narrow emission line at ~ 20 km s $^{-1}$, probably corresponding to the blue component of the doublet. We have also marked the corresponding position of the red component, assuming it is velocity shifted by the same amount. The red component seems to be present, but the absorption from H₂ prevents positive identification. Kaler et al. (1993) noticed similar narrow emission lines on top of the broad P-Cygni profiles in optical O VI features.

Table 1: The Program Objects

Name	PN G	R.A. (J2000)	Dec (J2000)	v_r^a (km s $^{-1}$)	PN Diameter ($''$)
NGC2371	189.1+19.8	07 25 34.71	+29 29 26.20	+20.6 \pm 2.7	48.9 \times 30.6 ^b
Abell 78	081.2-14.9	21 35 29.8	+31 41 40	+17 \pm 10.0	107 ^a
NGC 1535	206.4-40.5	04 14 15.9	-12 44 21	-3.2 \pm 1.4	33.3 \times 32.1 ^b
IC 4776	002.0-13.4	18 45 50.57	-33 20 32.94	+18.9 \pm 0.7	8.5 \times 4.0 ^b

a: Cahn & Kaler (1971)

b: Tylenda et al. (2003), two dimensions given.

Table 2: Utilized Spectra

Star	Instrument	Data-set	Date	Resolution	Aperture ($''$)	Range (Å)	Scale Factor
NGC 2371	FUSE	P1330301	02/26/00	\sim 0.05 Å	30 \times 30	915–1180	
	IUE	SWP04883	04/07/79	5–6 Å	10 \times 20	1180–1975	\times 1.3
	IUE	LWR04210	04/07/79	5–6 Å	10 \times 20	1975–3345	\times 1.3
Abell 78	BEFS	BEFS2190	12/01/96	\sim 0.33 Å	20	915–1222	
	IUE	SWP19906	05/05/83	\sim 0.2 Å	10 \times 20	1122–1975	\times 1.2
NGC 1535	FUSE	P1150808	10/05/01	\sim 0.05 Å	30 \times 30	915–1180	
	STIS+E140M	O64D04010	03/01/01	\sim 0.05 Å	0.2 \times 0.2	1180–1700	
IC 4776	FUSE	P1330501	05/21/00	\sim 0.05 Å	30 \times 30	915–1180	
	IUE	SWP16504	03/11/82	5–6 Å	10 \times 20	1180–1975	\times 1.25
	IUE	LWR12764	03/11/82	5–6 Å	10 \times 20	1975–3345	\times 1.25

Table 3: Model abundances (X_{\odot} = solar abundance)

Parameter	X_H	X_{He}	X_C	X_N	X_O	X_{Si}	X_S	X_{Fe}
NGC 2371	-	0.54	0.37	$\lesssim 0.01?$	0.08	X_{\odot}	X_{\odot}	$X_{\odot}?$
Abell 78	-	0.54	0.37	0.01	0.08	X_{\odot}	X_{\odot}	$\lesssim 0.03 X_{\odot}$
NGC 1535	X_{\odot}	X_{\odot}	X_{\odot}	X_{\odot}	X_{\odot}	X_{\odot}	X_{\odot}	X_{\odot}
IC 4776	X_{\odot}	X_{\odot}	X_{\odot}	X_{\odot}	X_{\odot}	X_{\odot}	X_{\odot}	X_{\odot}

?: Value uncertain, see text.

Table 4: H_2 and H I parameters

Star	Component	$\log N$	T	Note
NGC 2371	H I(IS+circ)	21.0	80	Not fit
	H_2 (IS)	$18.0^{+0.7}_{-0.3}$	80	
	H_2 (circ)	$17.0^{+0.3}_{-0.7}$	300	
Abell 78	H I(IS+circ)	$21.1^{+0.2}_{-0.2}$	80	From Ly α
	H_2 (IS)	$19.7^{+0.3}_{-0.7}$	80	
	H_2 (circ)	$16.4^{+0.3}_{-0.7}$	300	
NGC 1535	H I(IS+circ)	20.8 ± 0.1	80	From Ly α
	H_2 (IS)	$18.7^{+0.3}_{-0.7}$	80	
	H_2 (circ)	$16.4^{+0.3}_{-0.4}$	400	
IC 4776	H I(IS+circ)	$21.4^{+0.3}_{-0.4}$	80	From Ly β
	H_2 (IS)	$15.7^{+0.3}_{-0.7}$	80	
	H_2 (circ)	$15.7^{+0.3}_{-0.7}$	300	

Table 5. Nebular Parameters and Estimated Kinematic Ages

Name	n_e (cm $^{-3}$)	T_e (K)	$\log(F_{H\beta}^{obs})$ (ergs cm $^{-2}$ s $^{-1}$)	He/H	He $^{2+}$ /He $^{+}$	v_{exp} (O III) (km s $^{-1}$)	θ_{adopt} ($''$)	r_{neb} (pc)	τ_{dyn} (kyr)
NGC 2371	1260 ^a	14,100 ^b	-10.99 ^b	0.11 ^c	0.688 ^b	42.5 ^d	40	0.15	3.3
Abell 78	790 ^e	20,800 ^b	-12.04 ^b	0.110 ^b	1.61 ^b	27 ^f	107	0.42	15
NGC 1535	2100 ^g	10,800 ^g	-10.45 ^b	0.096 ^b	0.126 ^b	20 ^f	33	0.13	6.3
IC 4776	12,000 ^h	8600 ^{b,h}	-10.73 ^b (-10.43 ⁱ)	0.085 ^b	0.005 ^b	22 ^j	6	0.06	2.5

References. — (a): Feibelman (1997) (b): Cahn et al. (1992) (c): Kaler et al. (1993) (d): Sabbadin (1984) (e): Medina & Peña (2000) (inner knots, upper limit) (f): Weinberger (1989) (g): Tylenda et al. (1991) (h): Phillips (1998) (i): adopted, see text. (j): Gesicki & Zijlstra (2000)

Table 6: Reddening parameters

Star	E_{B-V} (UV slope) (mag)	E_{B-V} ($c_{H\beta}$) (mag)	E_{B-V} (H I) (mag)
NGC 2371	0.070 ± 0.02	0.07^a	-
Abell 78	0.100 ± 0.02	0.12^b	0.21
NGC 1535	0.055 ± 0.02	0.07^b	0.13 ± 0.03
IC 4776	0.090 ± 0.02	0.07^b	$0.52_{-0.21}^{+0.52}$

a: Kaler et al. (1993)

b: Cahn et al. (1992)

Table 7: Derived Stellar Parameters and Adopted Distances

Star	T_{eff}^\dagger (kK)	R_t^\dagger (R_\odot)	v_∞^\dagger ($km\ s^{-1}$)	D (kpc)	R_*^\dagger (R_\odot)	$\log L^\dagger$ (L_\odot)	$\log \dot{M}^\dagger$ ($M_\odot\ yr^{-1}$)	$\log \dot{M}^\ddagger$ ($M_\odot\ yr^{-1}$)	η^\dagger
NGC 2371	135_{-15}^{+10}	15_{-5}^{+10}	3700 ± 200	1.5^a	0.09	$3.45_{-0.20}^{+0.12}$	-7.11 ± 0.30	-10.6	5.0
Abell 78	113 ± 8	37_{-15}^{+20}	3200 ± 50	1.6^a	0.19	$3.73_{-0.13}^{+0.10}$	$-7.33_{-0.13}^{+0.36}$	-9.3	1.4
NGC 1535	66 ± 5	200_{-75}^{+100}	1950 ± 50	1.6^b	0.43	3.60 ± 0.13	-8.10 ± 0.30	-8.1	0.2
IC 4776	60_{-5}^{+10}	125_{-45}^{+105}	2300 ± 200	3.9^a	0.35	$3.20_{-0.15}^{+0.27}$	-7.85 ± 0.30	-8.8	1.0

(a): Cahn et al. (1992)

(b): Sabbadin et al. (1984)

†: From our spectral modeling.

‡: Predicted mass-loss rate for our derived parameters T_{eff} , L , $\log g$, v_∞ , using prescription of Vink et al. (2001).

Table 8: Derived Stellar Parameters From Evolutionary Tracks of Vassiliadis & Wood (1994)

Star	Track	M_c (M_\odot)	M_{init} (M_\odot)	τ_{evol} (kyr)	$\log g$ ($cm\ s^{-2}$)
NGC 2371	He	0.63	2	~ 13	6.3
Abell 78	He	> 0.63	> 2.0	$\lesssim 10$	5.7
NGC 1535	H	0.58	1.2	~ 15	4.9
IC 4776	He	0.57	1.0	~ 8	5.1

Table 9: Levels and superlevels for model ions

Element	I	II	III	IV	V	VI	VII	VIII	IX	X	XI
H	20/30	1/1									
He	40/45	22/30	1/1								
C		30/54	13/18	1/1							
N			29/53	13/21	1/1						
O			29/48	41/78	13/19	1/1					
Si			22/33	1/1							
P			36/178	16/62	1/1						
S			51/142	31/98	28/58	1/1					
Fe			51/294	47/191	44/433	41/254	53/324	52/490	43/210	1/1	